The major Late Albian transgressive event recorded in the epeiric platform of the Langshan Formation in central Tibet

YIWEI XU[1], XIUMIAN HU[1]*, MARCELLE K. BOUDAGHER-FADEL[2], GAOYUAN SUN[3], WEN LAI[1], JUAN LI[1] & SHIJIE ZHANG[1]

[1]*State Key Laboratory of Mineral Deposits Research, School of Earth Sciences and Engineering, Nanjing University, Nanjing 210023, China*

[2]*Department of Earth Sciences, UCL, Gower Street, London WC1E 6BT, UK*

[3]*College of Oceanography, Hohai University, Nanjing 210098, China*

**Correspondence: huxm@nju.edu.cn*

Abstract: Global sea-level changes strongly impact within-basin depositional patterns and the evolution of palaeoclimate, palaeogeography and palaeoecology. During the long, worldwide ice-free period in the mid-Cretaceous greenhouse time interval, high-frequency global sea-level changes were recorded in sedimentary archives. However, the causes of these global sea-level changes are still debated. In central Tibet, the 1 km-thick Langshan Formation has been dated to the late Aptian to early Cenomanian based on larger benthic foraminifera and accumulated in an epeiric seaway, thus, it provides a good opportunity to reconstruct the sea-level change and their controlling factors. Eleven distinct microfacies corresponding to three sedimentary environments have been identified in the Langshan Formation. Calcispheres marlstone and bioclastic wackestone with calcispheres were deposited in an open marine environment; coral rudstone, rudist rudstone and benthic foraminifera–rudist wackestone characterize were deposited in a rudist bank environment; and orbitolinids floatstone–rudstone, green algae packstone, bioclastic grainstone, orbitolinids wackestone with small benthic foraminifera, spicules wackestone and small benthic foraminifera wackestone–mudstone were deposited in a lagoonal environment. The Langshan Formation accumulated on an epeiric platform. This unit documents a sudden deepening event from a rudist bank to an open marine environment during the late Albian (*c.* 107 Ma). Integrating these findings with regional data from the literature, we infer that this deepening event was a widespread, roughly synchronous feature across the globe, and was controlled by a global sea-level rise related to the decay of polar ice sheets or the release of water from continental aquifers.

Supplementary material: Benthic and planktonic foraminifers in the Leitie and Zulong Sections are available at https://doi.org/10.6084/m9.figshare.c.4697147

It is generally accepted that global sea-level strongly impacts depositional patterns within sedimentary basins, biodiversity (Holland 2012), ocean circulation, oceanic anoxic events and various climate processes (Miller *et al.* 2005; Haq 2014). Global sea-level change is also important for evaluating ephemeral glaciations or other causative mechanisms (Ramkumar 2015). The mid-Cretaceous is considered to have featured an ice-free world with a greenhouse climate (Hay 2017; O'Brien *et al.* 2017; Huber *et al.* 2018), and well-preserved oceanic and epeiric strata during this time record several global sea-level cycles (Miller *et al.* 2005; Haq 2014). However, the causes of the eustatic sea-level changes during greenhouse times remain under debate (Miller *et al.* 2005; Haq 2014; Sames *et al.* 2016; Wendler & Wendler 2016; Hay 2017). The identification and history of global sea-level changes under a greenhouse climate are vital for understanding their causes.

Several Cretaceous eustatic sea-level reconstructions exist (Sahagian *et al.* 1996; Miller *et al.* 2005; Kominz *et al.* 2008; Müller *et al.* 2008; Haq 2014). However, those works are partly contradictory and need re-evaluation. For example, Müller *et al.* (2008) reconstructed long-term second-order eustatic sea-level change since 140 Ma by reconstruction of global seafloor age–area and depth–area distribution. Based on this curve, we cannot obtain third-order sea-level changes. The curves reconstructed by Sahagian *et al.* (1996), Miller *et al.* (2005) and Kominz *et al.* (2008) are firstly based on different regional data, and need to be tested to determine whether they represent global signals of sea-level changes. Additionally, those curves focus on only parts of the Cretaceous, e.g. Sahagian *et al.* (1996) on Early Cretaceous and Miller *et al.* (2005) and Kominz *et al.* (2008) on Late Cretaceous. Those curves show only limited overlap.

From: Wagreich, M., Hart, M. B., Sames, B. & Yilmaz, I. O. (eds) *Cretaceous Climate Events and Short-Term Sea-Level Changes*. Geological Society, London, Special Publications, **498**,
https://doi.org/10.1144/SP498-2019-8

Therefore, we need more data from other regions to test the validity of those curves. Haq (2014) replotted the Cretaceous sea-level curve by correlating synchronous sequence boundaries in several non-contiguous basins; however, some sequence boundaries are classified as provisional eustatic events that remain to be confirmed. Furthermore, these eustatic sea-level curves are partly compatible, for example, published estimates of the Late Cretaceous sea-level differ greatly by half an order of magnitude, from *c.* 40 to *c.* 250 m above the present level (Müller *et al.* 2008).

Direct measurement of the mid-Cretaceous sea-level is impossible because the sea-level at any one place is influenced by local tectonics. Epeiric seas are considered to be nearly ideal for precisely tracing eustatic change (Cisne *et al.* 1984; Cisne & Gildner 1988). With a low relief gradient (Heckel 1972), depth changes in an epeiric sea tend to reflect sea-level change rather than temporally shifting spatial gradients (Cisne & Gildner 1988). In addition, carbonate platforms, especially in such settings, are sensitive recorders of the relative sea-level over time (Immenhauser *et al.* 1999; Husinec & Jelaska 2006).

The thick shallow-marine carbonate successions of the central Tibet span the critical mid-Cretaceous interval and were deposited in an epeiric seaway with abundant index fossils (orbitolinids and rudists). Biostratigraphy based on larger benthic foraminifera, coupled with detailed microfacies analysis, allows us to place firm constraints on the stratigraphic and environmental evolution and sea-level change of the mid-Cretaceous and to discuss the factors controlling these sea-levels during this critical greenhouse climate time interval.

Geological settings

Lhasa terrane

The Lhasa terrane, a part of the Tibet Plateau, lies between the Indus–Yarlung suture to the south and the Bangong–Nujiang suture to the north. This terrane consists of the southern Lhasa subterrane and the northern Lhasa subterrane which are divided by the Luobadui–Milashan Fault (Fig. 1a) (Burg *et al.* 1983; England & Searle 1986; Yin & Harrison 2000; Pan *et al.* 2004). The southern Lhasa subterrane mainly comprises the Xigaze forearc basin and the Gangdese arc, which were influenced by the subduction of Neo-Tethys oceanic crust (Yin & Harrison 2000). The Gangdese arc began uplifting at *c.* 113 Ma and provided detrital materials to the Xigaze forearc basin (Wang *et al.* 2017*a*). The northern Lhasa subterrane mainly comprises Paleozoic metasedimentary rocks, Jurassic–Cretaceous sedimentary strata and Mesozoic igneous rocks (Fig. 1b). During the mid-Cretaceous, the marine strata of the northern Lhasa subterrane were mainly deposited within an epeiric seaway, which was located at a palaeolatitude of *c.* 20° N (DeCelles & Kapp 2007; Leier *et al.* 2007*a*, *b*; Chen *et al.* 2012; Ma *et al.* 2018). This epeiric seaway opened to the Neo-Tethys ocean to the west and was bounded by Cretaceous continental strata to the north (DeCelles & Kapp 2007) and to the east (Wang *et al.* 2017*b*), and by Cretaceous volcanic rocks to the south which provided detrital materials to the seaway (Sun *et al.* 2017; Lai *et al.* 2019*b*).

Stratigraphy

The Cretaceous strata in the northern Lhasa subterrane include the Duoni, Langshan and Jingzhushan/Daxiong formations (Pan *et al.* 2004; Zhang *et al.* 2004). The Duoni Formation is dominated by sandstone with interbedded conglomerate and mudstone interpreted to have been deposited within deltaic to fluvial environments (Leier *et al.* 2007*a*, *c*; Zhang *et al.* 2011; Sun *et al.* 2017; Lai *et al.* 2019*b*). The depositional age of the Duoni Formation is constrained by geochronologically dated tuff layers from 123 to 116 Ma (Sun *et al.* 2017).

Conformably overlying the Duoni Formation, the Langshan Formation is widely distributed in the northern Lhasa subterrane from east to west, with a length of *c.* 1200 km (Fig. 1b), and mainly comprises thick-bedded bioclastic limestone interbedded with sandstone, mudstone and marlstone (Zhang 2000; Zhang *et al.* 2004, 2012; Leier *et al.* 2007*a*; Sun *et al.* 2017). The age of the Langshan Formation was previously constrained by fossil assemblages to Aptian–Albian (DeCelles & Kapp 2007; Leier *et al.* 2007*a*), Aptian–early Cenomanian (BouDagher-Fadel *et al.* 2017) or Barremian–early Cenomanian (Rao *et al.* 2015).

The Jingzhushan Formation exposed to the north of the outcrop belt of the Langshan Formation mainly consists of red conglomerate and coarse sandstone, interbedded with siltstone. The Daxiong Formation is characterized by a set of conglomerates distributed to the south of the area of the Langshan Formation. Both the Jingzhushan and Daxiong formations are interpreted to have been deposited in alluvial fan environments. The tuff layers within these formations constrain the onset of deposition at *c.* 92 Ma, indicating the initial uplift of the northern Lhasa terrane at *c.* 92 Ma (Sun *et al.* 2015; Lai *et al.* 2019*a*).

Materials and methods

Samples were collected from three stratigraphic sections (Fig. 1b). Among them, the Azhang section (GPS: 31° 52′ 48.5″ N, 84° 55′ 16.5″ E) and

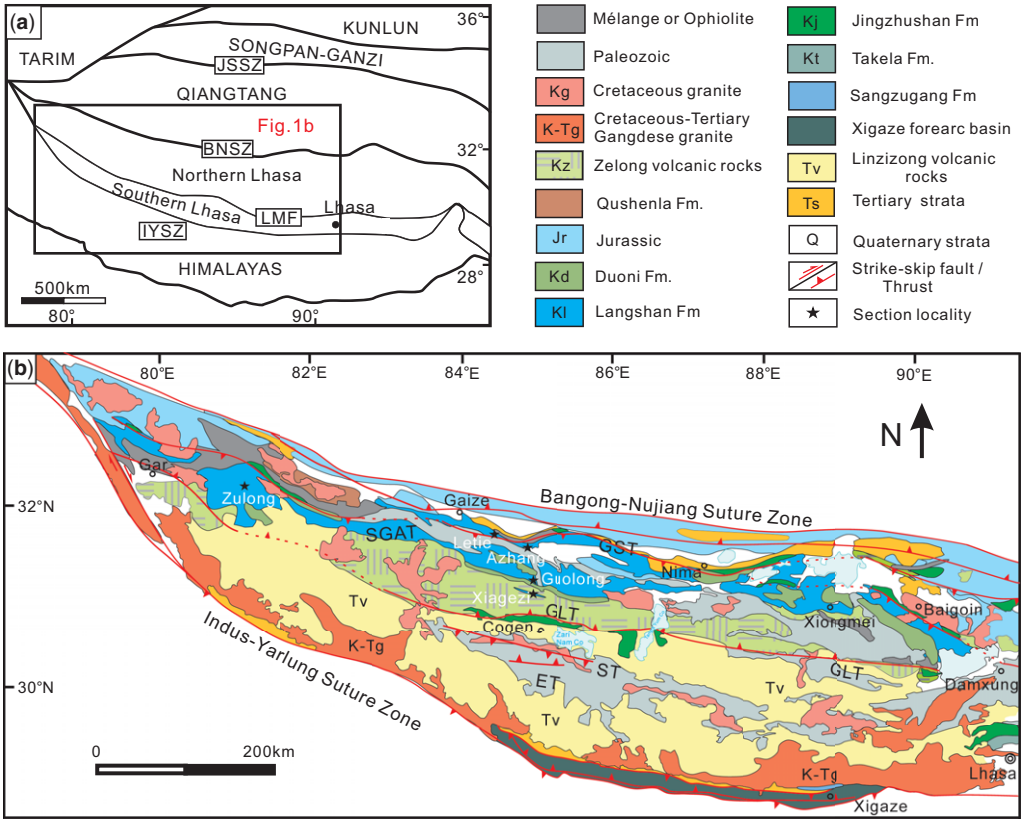

Fig. 1. (**a**) Simplified tectonic map of the Tibetan Plateau and adjacent regions (Pan *et al.* 2004). JSSZ, Jinsha suture zone; BNSZ, Bangong–Nujiang suture zone; LMF, Luobadui–Milashan Fault; IYSZ, Indus–Yarlung suture zone. (**b**) Simplified geological map of the Lhasa Basin, showing the studied section Lhasa terrane (modified after Pan *et al.* 2004). GST, Gaize-Selin Co thrust; SGAT, Shiquan–Gaize–Amdo thrust; GLT, Gugu La thrust; ST, Shibaluo thrust; ET, Emei La thrust. The localities of the Guolong and Xiagezi sections are from BouDagher-Fadel *et al.* (2017).

the Zulong section (GPS: 32° 36′ 38.64″ N, 81° 19′ 47.95″ E) are well exposed and were systemically sampled, whereas the Langshan Formation in the Letie section (GPS 32° 5′ 20.476″ N, 84° 27′ 57.114″ E) is partly covered. The sampling frequency is *c.* 2–4 m per sample. A total of 643 samples were employed for thin section and further microfacies analysis.

In this study, foraminifera species were studied in thin sections under a polarizing microscope. Based on the foraminifera assemblage, the benthic foraminiferal zones are defined and correlated to the established Tibetan Larger Benthic Foraminiferal biozones of the Cretaceous (TLK1) by BouDagher-Fadel *et al.* (2017). The eight identified foraminiferal biozones (TLK1a-h) are Aptian to early Cenomanian in age and were used to correlate the South Tibetan sedimentary successions. These biozones are defined as follow: (1) TLK1a corresponds to planktonic foraminifera biozone (PZ) Aptian 1–2 and is dominated by *Palorbitolina* and *Praeorbitolina* spp.; (2) TLK1b corresponds to PZ Aptian 3 and is characterized by the first appearance of *Mesorbitolina parva*; (3) TLK1c of Late Aptian (PZ Aptian 4) age is characterized by the first appearance of *Mesorbitolina texana*; (4) TLK1d of Albian (PZ Albian 1) age is defined by the first appearance of *Cuneolina pavonia*; (5) TLK1e of Albian (PZ Albian 2) age is characterized by the first appearance of *Palorbitolinoides hedini*; (6) TLK1f of Middle Albian (PZ Albian 3) age and is characterized by the first appearance of *Mesorbitolina aperta*; (7) TLK1g of end Albian (PZ Albian 4) age is characterized by the appearance of *Conicorbitolina* cf. *cuvillieri* and *Pseudochoffatella cuvillieri*; and (8) TLK1h of Early Cenomanian age is characterized by the first appearance of *Conicorbitolina* sp. A and *Nezzazata conica*. The foraminiferal assemblages in this study are correlated with these biozones and were further correlated with the planktonic foraminiferal

bioevents in the Late Mesozoic as defined by BouDagher-Fadel (2015) and calibrated against the biostratigraphic time scale and chronostratigraphy (as defined by Gradstein *et al.* 2012 and revised by Cohen *et al.* 2013) (Fig. 2b).

Microfacies analysis was performed by examining the mineralogical components, macrofossil and microfossil assemblages and textures of the samples observed in thin sections and outcrops. Fossil or fossil debris such as green algae, benthic foraminifera and planktonic foraminifera were identified without taxonomic details in thin sections to determine depositional environment. Carbonate rocks in the thin section were described based on the Dunham (1962) and Embry & Klovan (1971) classifications of carbonate rocks. Major fossil groups were determined using the descriptions and photographs in Flügel (2010). For the determination of the depositional environments, microfacies models of Wilson (1975) and Flügel (2010) were used.

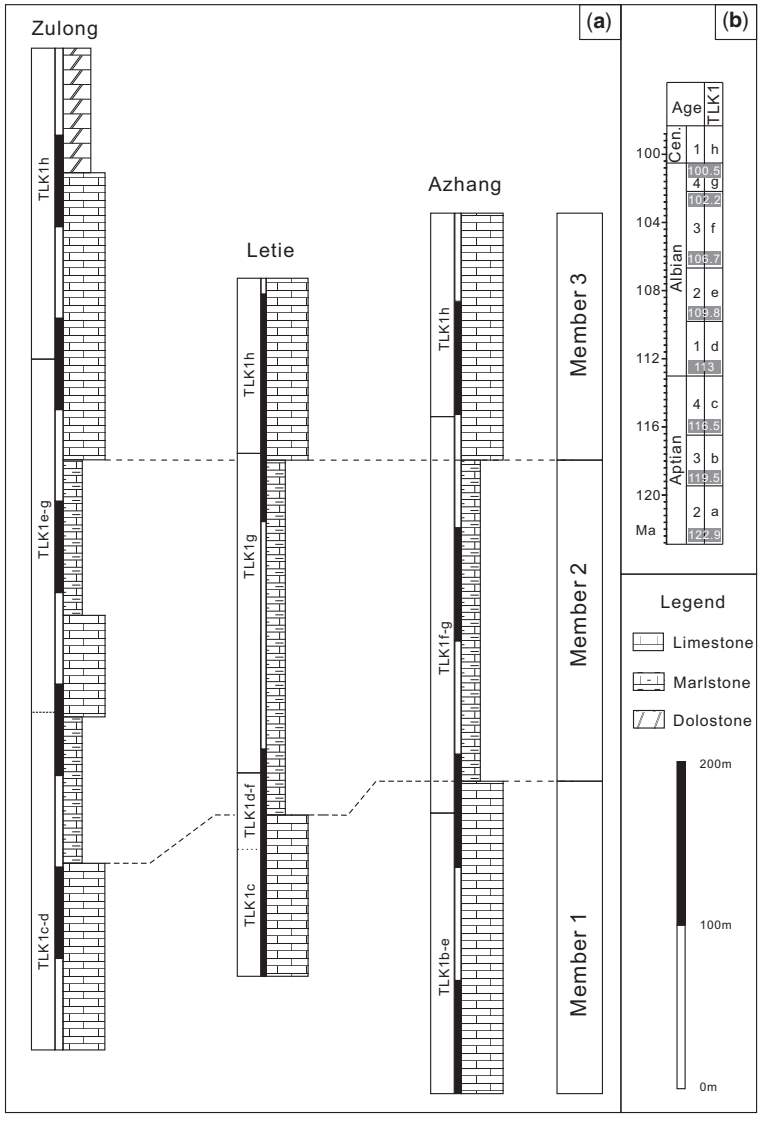

Fig. 2. (**a**) Lithology and biostratigraphic correlation of three sections of the Langshan Formation. (**b**) Larger benthic foraminiferal biozones and their age (modified after BouDagher-Fadel *et al.* 2017). Abbreviation: Cen., Cenomanian; TLK1, Tibetan Larger foraminiferal zones of the Cretaceous.

Results

Lithostratigraphy and biostratigraphy

The Langshan Formation can be further subdivided into three members (Fig. 2a). Member 1 comprises thick-bedded black bioclastic limestone with thicknesses of *c.* 230 m in the Azhang section, *c.* 72 m in the Letie section and 200 m in the Zulong section. Member 2 comprises thinly bedded grey marlstone interbedded with several beds of limestone with thicknesses of 260 m in the Azhang section, 315 m in the Letie section and 420 m in the Zulong section. In the Zulong section, Member 2 can be divided into three parts based on its lithology. The lower and upper parts of Member 2 are grey marlstones, and the middle part consists of black limestone. The contacts of Member 2 with both underlying Member 1 and overlying Member 3 are conformable. Member 3 comprises black bioclastic limestone with thickness *c.* 200 m in the Azhang section and *c.* 150 m in the Letie section. Member 3 comprises limestone and dolostone with thickness of *c.* 400 m in the Zulong section.

The biostratigraphy of the Azhang section is described in detail in BouDagher-Fadel *et al.* (2017). Here we provide an overview of the biozones of the Azhang section. The age of Member 1 spans Aptian 3–Albian 3 (119.5–102.2 Ma) (BouDagher-Fadel *et al.* 2017). Member 1 of the Azhang section contains *Sabaudia capitata*, *Palorbitolina lenticularis*, *Mesorbitolina parva* and *Palorbitolinoides hedini*, indicating an age of Aptian 3–Albian 2 (119.5–106.7 Ma) (BouDagher-Fadel *et al.* 2017). *Palorbitolinoides hedini* is absent in the uppermost portion of Member 1 where *Mesorbitolina aperta* makes its first appearance. The latter also occurs in Member 2, indicating an age of Albian 3 for uppermost Member 1 and Member 2 (BouDagher-Fadel *et al.* 2017). Member 3 contains *Ascoliella quadrata*, *Conicorbitolina* cf. *cuvillieri*, *Pseudochoffatella* sp. B, *Nezzazata conica* and *Daxia cenomana*, indicating an age of Albian 4–Cenomanian 1 (102.2–98.8 Ma) (BouDagher-Fadel *et al.* 2017).

In this study, we mainly focus on the orbitolinids and planktonic foraminiferal biozones in the Letie (Fig. 3) and Zulong sections (Fig. 4). The occasional coexistence of planktonic foraminifera with the larger benthic foraminifera enables the stratigraphic ranges of the latter to be defined very precisely, as they can be tied to the high-resolution planktonic zonal dating scheme of BouDagher-Fadel (2015, 2018*a*, *b*), which itself is correlated to the absolute time scale of Ogg & Hinnov (2012) and Cohen *et al.* (2013).

In the Letie section, Member 1 contains orbitolinid index fossils like *Mesorbitolina parva, Palorbitolina lenticularis* (Plate 1, Fig. 3) and *Vercorsella arenata* (Plate 1, Fig. 7), indicating an age of Aptian 4 (116.5–113 Ma). The *Favusella washitensis* (Plate 1, Fig. 6) makes its first appearance in the uppermost portion of Member 1, indicating an age of latest Aptian (Aptian 4)/Albian at this level. The occurrence of *Hedbergella rischi* at the bottom of Member 2 confirms the Albian age. Rare planktonic foraminifers are present in the lower part of Member 2 while the boundaries among the planktonic foraminiferal biozones of Albian 1–3 are not clearly defined; however, planktonic foraminiferal index fossils of *Ascoliella quadrata* (Plate 1, Fig. 2) appear in the middle part of Member 2 indicating an age of Albian 4 (102.2–100.5 Ma). Thus, the age of Member 2 is Albian and the age of its middle part is Albian 4. In Member 3, the presence of *Trocholina altispira* indicates already a Cenomanian age.

In the Zulong section, Member 1 contains the orbitolinid index fossils *Vercorsella arenata* (Plate 2, Fig. 1), *Palorbitolina lenticularis* (Plate 2, Fig. 2), *Mesorbitolina parva, Orbitolinopsis* sp. A and *Cuneolina pavonia*, indicating an age from Aptian 4 to Albian 1 (116.5–109.8 Ma). In the middle part of Member 2, *Mesorbitolina subconcava* (Plate 2, Fig. 5) and *Mesorbitolina birmanica* (Plate 2, Fig. 6) are common. The disappearance of the index fossil *Palorbitolinoides orbiculata* (Plate 1, Fig. 3) in this interval indicates an age of Albian 2–3 (109.8–102.2 Ma). In Member 3, the presence of *Praeorbitolina* cf. *wienandsi* and *Orbitolina qatarica* indicates an age of Albian 4 to Cenomanian 1 (102.2–98.8 Ma). Considering the age of Members 1 and 3, we infer that the age of Member 2 is Albian 1–4 (116.5–100.5 Ma), specifically, Albian 1 in the lower part and Albian 2–4 in the upper part.

The age range of Member 1 in the Azhang section is Aptian 3–Albian 3, which is greater than the age range of the others (Fig. 2a). The onset of deposition of Member 2 in the Zulong section was Albian 1, which is earlier than the others. In the Azhang and Letie sections, the age of Member 2 is Albian 3 to Albian 4, which can be correlated with the upper part of the marlstone of Member 2 in the Zulong section. The age of Member 3 in all studied sections is from Albian 4 to Cenomanian 1.

Microfacies

In the present study, we have recognized 11 microfacies, documenting three different depositional environments: lagoon, rudist bank and open marine (Table 1).

Open marine

MF1 Calcispheres marlstone. MF1 is described as a grey marlstone in outcrop and is found in

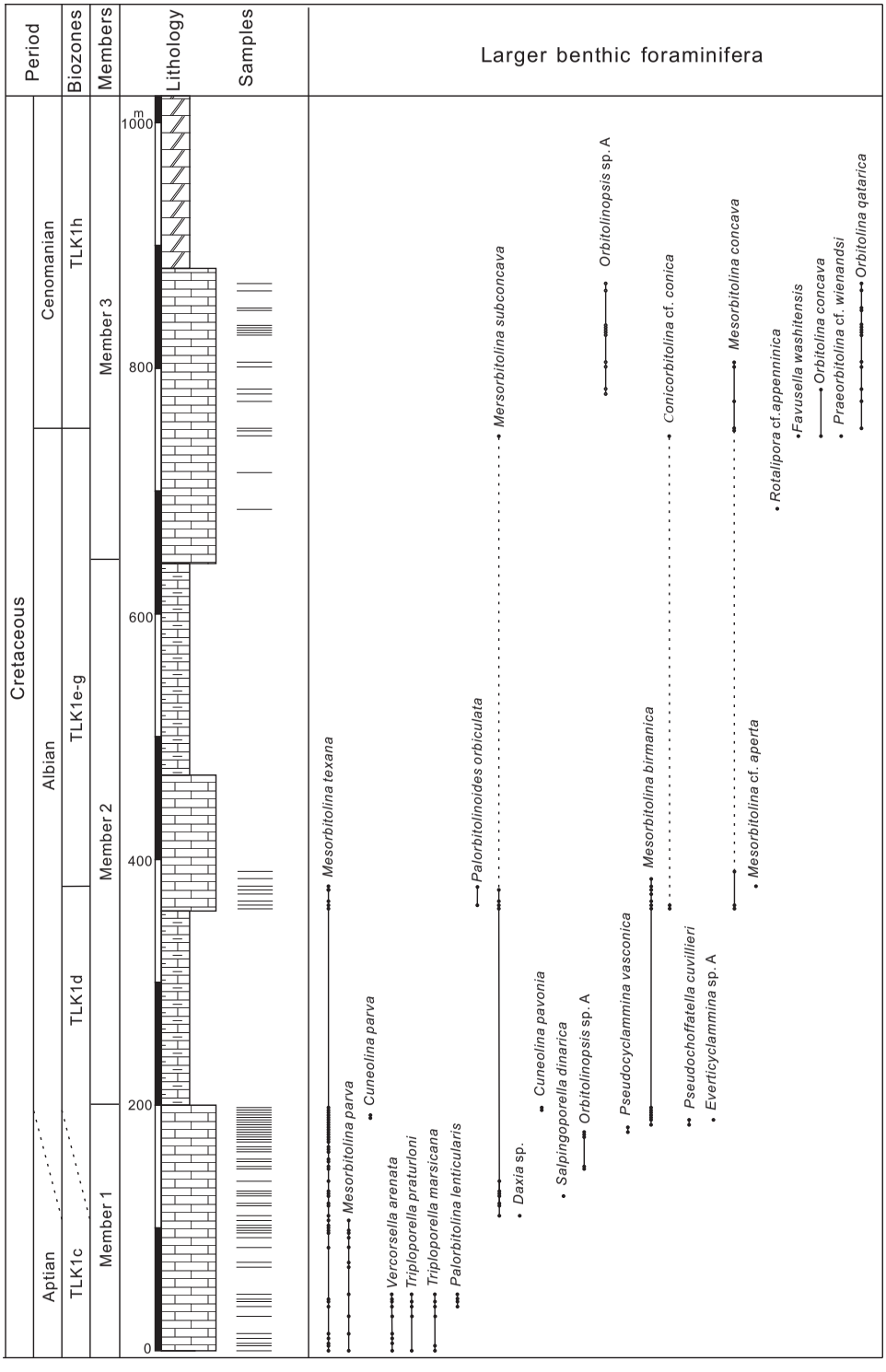

Fig. 3. Stratigraphy of the Langshan Formation in the Zulong section, showing the sample positions and occurrence of larger benthic foraminifera.

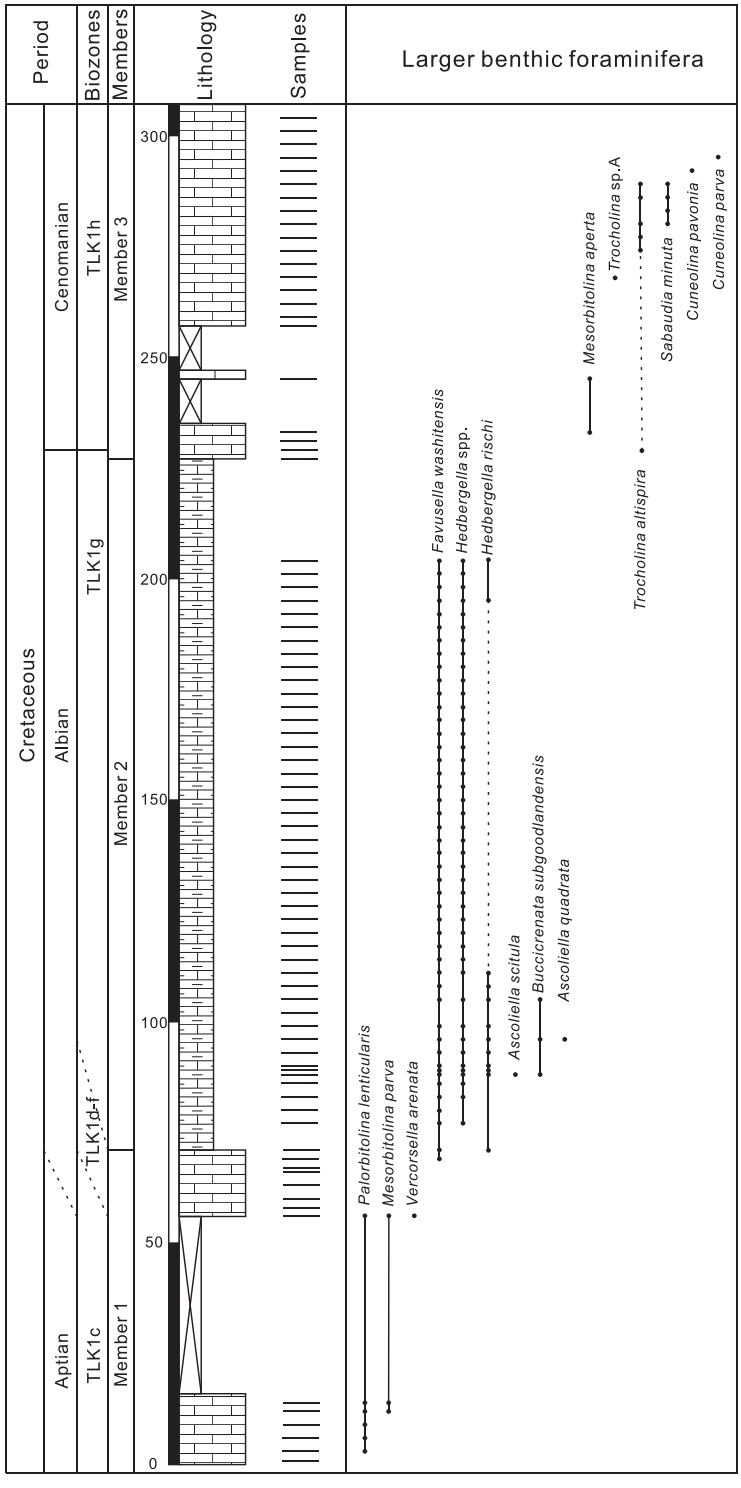

Fig. 4. Stratigraphy of the Langshan Formation in the Letie section, showing the sample positions and occurrence of larger benthic foraminifera.

Table 1. *Summarized characteristics of determined microfacies types in the Langshan Formation compared with the standard microfacies types after Flügel (2010)*

Microfacies	Microfacies name	Components		Structures	Depositional environment	Palaeodepth	Standard microfacies Flügel (2010)
		Skeletal	Non-skeletal				
MF1	Calcispheres marlstone	Calcispheres, minor planktonic foraminifera, rare echinoderms and ostracod	Silts	None	Open marine	50–100 m	SMF 3
MF2	Bioclastic wackestone with calcispheres	Planktonic foraminifera, calcispheres, echinoderms, bivavles, rare bryozoans and textulariids	None	None	Open marine	50–100 m	SMF 2
MF3	Coral rudstone	Coral debris, minor bivalve debris, sponge spicules, echinoiderms, rare ostracod, *Bacinella*, *Lithocodium*	Peloids	Boring	Forebank	>10 m	SMF 6
MF4	Rudist rudstone	Rudist and its debris, minor green algae debris, orbitolinids, echinoderms, minor *Bacinella*, *Lithocodium*, rare small textulariids, miliolids	Peloids	Boring	Rudist bank to forebank	0–5 m	
MF5	Benthic foraminifera–rudist wackestone	Rudist debris, bivavle, green algae, small miliolids and textulariids, minor *Bacinella, Lithocodium*, echoinoids, rare red algae	Peloids	None	Backbank	5–10 m	
MF6	Orbitolinids floatstone	Orbitolinids, fine bioclastic debris, rare textulariids, ostracod	Silts, peloids	None	Lagoon	10–50 m	SMF 18
MF7	Green algae packstone	Dasyclad, Halimeda, common textulariids and miliolids, minor orbitolinids, bivavle, rare echinoderms, gastropods, bryozones	None	None	Shallow lagoon	5–10 m	SMF 18
MF8	Bioclastic grainstone	Bivalves, rudist, orbitolinids, green algae, minor textulariids, miliolids bryozoans, rare echinoiderms, gastropods, red algae	Peloids, ooids, intraclasts	None	Shoal	0–10 m	
MF9	Orbitolinids wackestone with small benthic foraminifera	Orbitolinids, common textulariids, miliolids, green algae, rare *Bacinella*, *Lithocodium*, echinoiderms	Peloids	None	Shallow lagoon	0–10 m	SMF 18
MF10	Spicules wackestone	Sponge spicules, green algae, miliolids, other small benthic foraminifera	Peloids	None	Shallow lagoon	0–10 m	
MF11	Small benthic foraminifera wackestone–mudstone	Diverse small textulariids and miliolids, minor dasyclads, sponge spicules, orbitolinids	Peloids	Dissolution cavities	Shallow lagoon	0–10 m	SMF 18

Member 2 in the three studied sections. This facies is characterized by its micritic matrix that contains mainly calcispheres with minor planktonic foraminifera (Fig. 5a). The calcispheres (*c.* 30%) are *c.* 30 μm in diameter and filled by sparite. Non-keeled planktonic foraminifers represent less than 10% of the content. The matrix is micrite with minor silty quartz.

Calcispheres occur in pelagic limestone during the Jurassic and Cretaceous periods (Flügel 2010). The non-keeled planktonic foraminifera indicate a shallow shelf sea, with water depth of *c.* 50–100 m

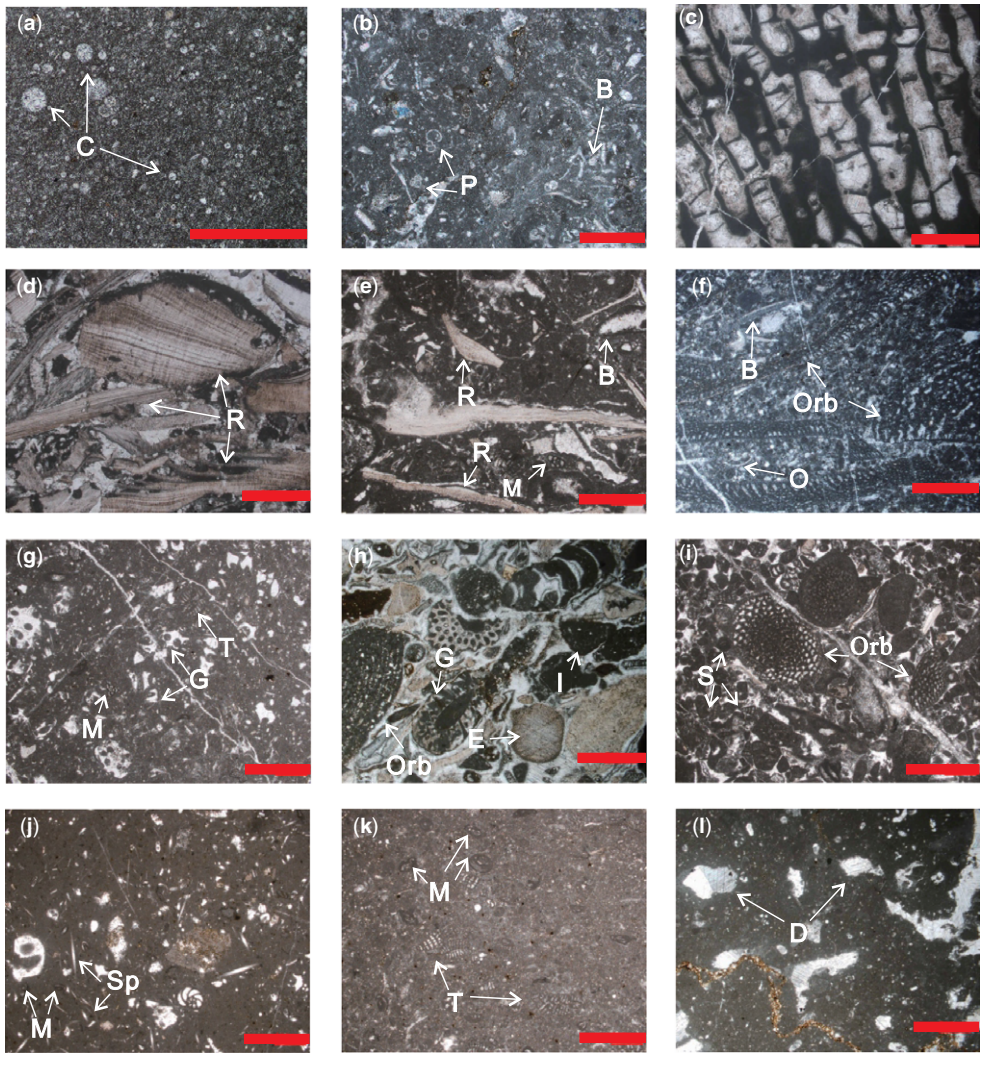

Fig. 5. (**a**) MF1. Calcispheres marlstone, sample 12ls76. C, Calcispheres. (**b**) MF2. Bioclastic wackestone with calcispheres, sample 17lt23. B, Bivalve; P, planktonic foraminifera. (**c**) MF3. Coral rudstone, sample 16zl160. (**d**) MF4. Rudist rudstone, sample 16zl232. R, Rudist. (**e**) MF5. Rudist packstone with Benthic foraminifera–rudist wackestone, sample 12ls54. R, rudist; B, bivalve; M, miliolid. (**f**) MF6. Orbitolinids rudstone, sample 16zl97. B, Bivalve; Orb, orbitolinids; O, ostracod. (**g**) MF7. Green algae wackestone, sample 12ls48. G, Green algae; M, miliolid; T, textulariid. (**h**) MF8. Bioclastic grainstone, sample 16zl126. E, Echinoderm; G, green algae; I, intrtaclast; Orb, orbitolinids. (**i**) MF9. Orbitolinids wackestone with small benthic foraminifera, sample 12ls47. Orb, Orbitolinids; S, small benthic foraminifera. (**j**) MF10. Spicules wackestone, sample 12ls32. M, Miliolid; Sp, sponge spicules. (**k**) MF11 Benthic foraminifera wackestone, sample 12ls27. M, Miliolid; T, Textulariid. (**l**) Dissolution cavities, sample 16zl106. D, Dissolution cavity. The scale bar represents 1 mm.

(Gold *et al.* 2017). The micritic matrix in association with pelagic organisms indicates a low-energy open marine environment; it can be correlated to SMF3 of Flügel (2010).

MF2 Bioclastic wackestone with calcispheres. This microfacies contains 10–20% carbonate grains with matrix supported texture. The components of the carbonate grains are mainly bivalve debris, accounting for *c.* 10% of the content, with minor amounts of calcispheres and planktonic foraminifers, accounting for 5% of the content. Echinoderms are also present (Fig. 5b). This microfacies is restricted to Member 2 of the Azhang and Letie sections.

Planktonic foraminifera and calcispheres usually developed in hemi-pelagic to pelagic environments (Flügel 2010). The bivalve and echinoderm debris are inferred to have been transported from shallower environments during episodic high-energy storm events or other gravity flow events, and we interpreted this microfacies as an open marine environment affected by storms or deposited at the toe of a slope. This microfacies can be correlated to SMF2 of Flügel (2010).

Coral and rudist bank

MF3 Coral rudstone. This microfacies contains 50–70% carbonate grains with grain-supported texture. Coral debris is the main component (40–50%), with a diameter of *c.* 0.5–2 cm. The corals were bored by encrusters. Peloids occur among the coral debris with *c.* 15% content. Bivalve debris accounts for 5% of the content (Fig. 5c). This microfacies occurs in the Zulong and Letie sections.

The assemblage of corals and rudists usually lived in an outer platform environment during the Cretaceous (Zaghbib-Turki 2003), and corals always occurred in relatively deeper water than rudists (Gili *et al.* 1995; Fernández-Mendiola *et al.* 2013). Combined with its stratigraphic relationship with MF4, MF3 is interpreted to be a carbonate fore-bank sourced from nearby patch reefs, and it can be correlated to SMF6 of Flügel (2010).

MF4 Rudist rudstone. This microfacies contains 70–80% carbonate grains and has a grain-supported texture. Grains of rudist debris up to 5 mm in diameter are the most abundant (60%). The rudist debris is poorly rounded. Some grains have been bored by microorganisms, and some have micritic envelopes. Some grains are coated by *Lithocodium* and *Bacinella*. Minor components include bivalves and orbitolinids, accounting for 10% of the content. Peloids can account for up to 10%. Red algae, green algae, echinoderm and gastropods are rare. The micritic matrix represents *c.* 20–30% of the content (Fig. 5d). This microfacies occurs in the Zulong and Letie sections.

Rudists are traditionally regarded as typical infralittoral markers (Masse 1992). The poorly rounded rudist debris indicates a relatively short transport distance and high-energy conditions. Abundant debris with micritic envelope are common in platform-margin shoals (Flügel 2010). The micritic matrix may be a product of sheltering by large rudist debris or trapping by microorganisms, such as *Lithocodium* and *Bacinella*. This microfacies is interpreted to have formed in a rudist bank to fore-bank at a depth of *c.* 1.5–4.5 m (Alsharhan 1995).

MF5 Benthic foraminifera–rudist wackestone. This microfacies is matrix supported and has fewer than 40% carbonate grains. The grains are dominated by rudist and bivalve debris (20%) with diameters of *c.* 0.5–2 mm. *Lithocodium* and *Bacinella* coatings are common. Small benthic foraminifers (mainly textulariid and miliolid) account for 5–7% of the content, and orbitolinids account for *c.* 5%. Green algae, echinoderms and red algae are rare (Fig. 5e). This microfacies occurs widely in the studied sections.

The rudist clasts are finer than those in MF3a, indicating transport over a longer distance. The occurrence of *Lithocodium* and *Bacinella* indicates a shallow reef crest or lagoonal environment (Stein *et al.* 2012; Kaya & Altıner 2015). The green algae, miliolids and textulariids indicate a shallow water depth. Thus, this microfacies was suggested to have been deposited in a shallow-water environment behind a rudist bank.

Lagoon

MF6 Orbitolinids floatstone. This microfacies is matrix-supported or grain-supported and has a wide range of carbonate grain contents from 20 to 40%. Orbitolinids, 10–25% of the content, comprise the dominant grain type. The orbitolinids including conical and discoidal forms are well preserved. Subordinate grains include fine bivalve debris, accounting for 5% of the content. Small benthic foraminifera, sponge spicules, echinoderms and silt-sized quartz grains are rare. The matrix contains abundant peloids, with contents of up to 10% (Fig. 5f). This microfacies occurs in the Zulong and Azhang sections.

Orbitolinids live in a shallow water with depths of *c.* 10–50 m (Banner & Simmons 1994). Abundant peloids and carbonate mud in the matrix usually occur in lagoonal environments and indicate low energy conditions (Tucker & Wright 1990). This microfacies can be correlated with SMF18 (Flügel 2010). Thus, MF6 is interpreted to have been deposited in an open lagoon environment with *c.* 10–50 m water-depth.

MF7 Green algae packstone. This microfacies contains 20–60% carbonate grains with matrix or grain-supported texture. The green algae in this

microfacies consists of dasyclads and Halimeda-type algae (20–40%) and is occasionally coated by a micritic envelope. Orbitolinids, bivalve and echinoderm are subordinate (15%). Other grains include textulariids and miliolids (3–5%), gastropods and sponge spicules (Fig. 5g). This microfacies occurs widely in the studied sections.

Dasyclads are abundant in euphotic water of 5–10 m depth with normal salinity (Banner & Simmons 1994). A micritic matrix indicates a low-energy environment. This microfacies can be correlated with SMF18 (Flügel 2010). The water depth of this microfacies is probably 5–10 m, which is shallower than that of MF6. Thus, MF7 is interpreted to have been deposited in an open lagoon environment with water-depth *c.* 5–10 m.

MF8 Bioclastic grainstone. This microfacies contains 80% carbonate grains with grain-supported texture. The cement is composed of sparite. Bioclastic grains (50–60%) mainly consist of rounded orbitolinids, rudist with a micritic envelope, dasyclads and benthic foraminifera. Gastropod, echinoderm, red algae and bryozoan are subordinate. Non-skeletal grains including ooids and peloids account for 10–25% of the content (Fig. 5h). This microfacies occurs only in the Zulong and Azhang sections and is flanked by MF7 and MF11.

Oriented bioclasts and the absence of micrite in the matrix indicate a strong current. The occurrence of dasyclads and ooids suggests water depths less than 10 m (Flügel 2010). Considering that this microfacies is associated with MF5 and MF7, we interpreted it to have been deposited in a bioclastic shoal in the lagoon.

MF9 Orbitolinids wackestone with small benthic foraminifera. This microfacies contains 10–40% carbonate grains with matrix-supported texture. Orbitolinids (30%) and other small benthic foraminifera (5–10%) are abundant. Dasyclads and bivalves are rare, accounting for less than 5% of the content (Fig. 5i). This microfacies is adjacent to MF7 and MF11 and restricted to the Azhang section.

The co-occurrence of orbitolinids and other small benthic foraminifera indicates a shallower environment than for MF6. Abundant benthic foraminifera indicate a shallow lagoonal environment (Ghabeishavi *et al.* 2010). The dasyclads also indicate a shallow-water environment. Therefore, a shallow lagoonal environment is suggested for this microfacies and it can be correlated to SMF18 (Flügel 2010).

MF10 Spicules wackestone. The microfacies is characterized by wackestone with a micritic matrix (Fig. 5j). Carbonate grains constitute 25% of the content, and sponge spicules with a single axis are the most common components (10% of the content). Green algae debris (10%) constitute the subordinates. The miliolids account for 5%, and other benthic foraminifera have minor contents. This microfacies is only present in the Azhang section and occurs adjacent to MF7 and MF11.

The abundance of micrite represents a low-energy environment. The rich sponge spicules are interpreted to imply a deep-water or basin environment (Wilson 1975). However, based on modern sponge distributions, the spicules could also have originated in shallow-marine shelf and near-coast environments (Flügel 2010). In the studied thin sections, the co-occurrence of spicules and green algae implies shallow water. Combining its stratigraphic relationship with MF7 and MF11, the MF10 was suggested to have been deposited in a shallow lagoon environment.

MF11 Small benthic foraminifera wackestone–mudstone. The microfacies is characterized by a micritic matrix-supported texture with a 25% content of carbonate grains (Fig. 5k). The most common components are mainly small benthic foraminifera including miliolids and textulariids (5–15%), with minor green algae, sponge spicules, gastropod and echinoderms. The matrix is micrite, and in some parts, dissolution cavities are present (Fig. 5l). This microfacies occurs in the Zulong and Azhang sections.

Abundant miliolids and textulariids indicate shallow and restricted environments with water depths not exceeding 10 m (Davies *et al.* 2002). Micritization of miliolids also indicates a restricted, quiet environment favouring boring microorganisms (Tucker & Wright 1990). The exposure structure (dissolution cavities) also indicates a shallow water environment. Thus, MF11 is interpreted to have been deposited in a restricted shallow lagoon environment. This microfacies can be correlated with SMF18 (Flügel 2010).

Discussion

Palaeoenvironmental evolution of the Langshan Formation

Based on the biostratigraphy, microfacies and interpreted water depth, we reconstructed the history of palaeowater depth changes in the Langshan Formation (Figs 6–8).

Member 1 is dominated by abundant green algae and benthic foraminifera (MF7, MF9 and MF11) and deposited in a shallow lagoonal environment with water depths of no more than 10 m in the Azhang section (Fig. 8). In the Letie section rudist rudstone (MF4) and benthic foraminifera–rudist wackestone (MF5) indicate a rudist bank or back bank environment (Fig. 7). Additionally, Member 1 is dominated by rudist rudstone (MF4) and benthic

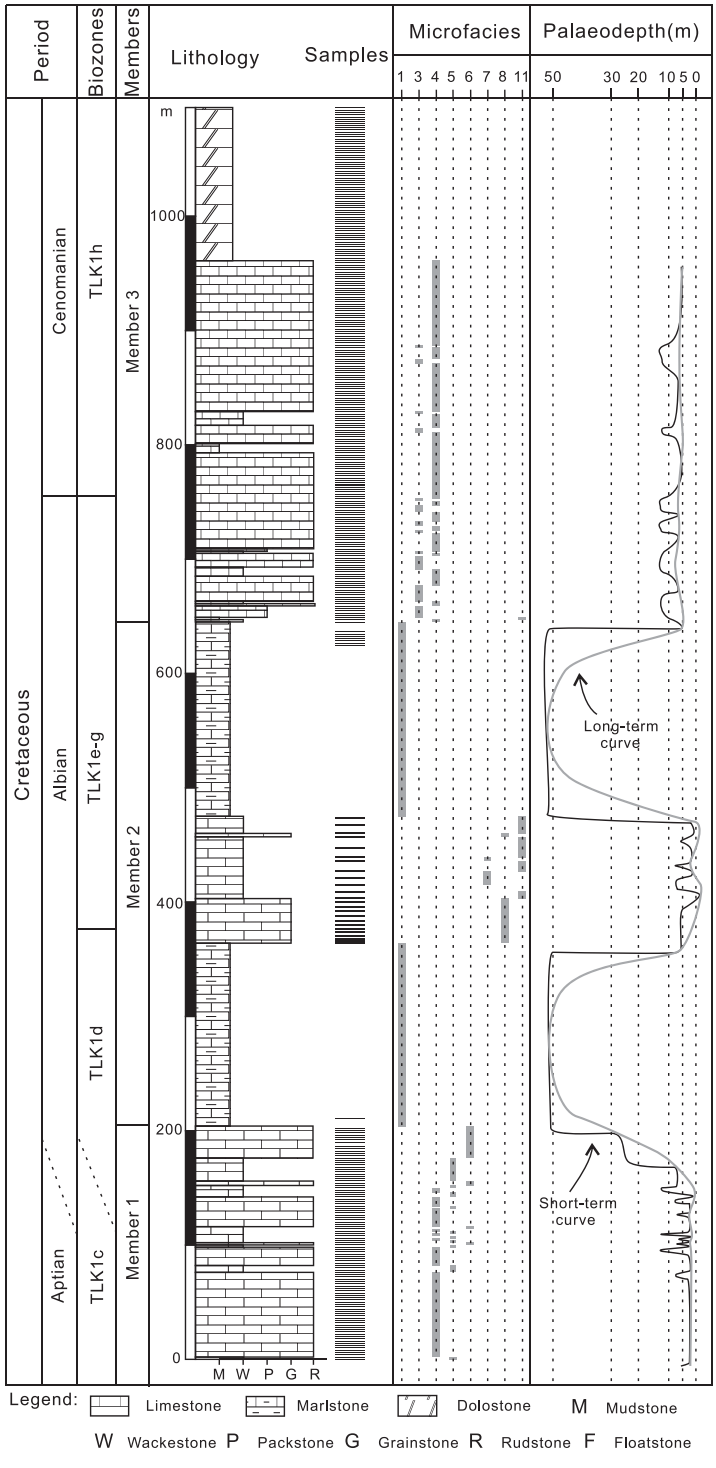

Fig. 6. Stratigraphy and microfacies distribution of the Langshan Formation in the Zulong section. In the columns, facies numbered 1–11 refer to the different microfacies. See the text for the descriptions and palaeodepths of microfacies 1–11.

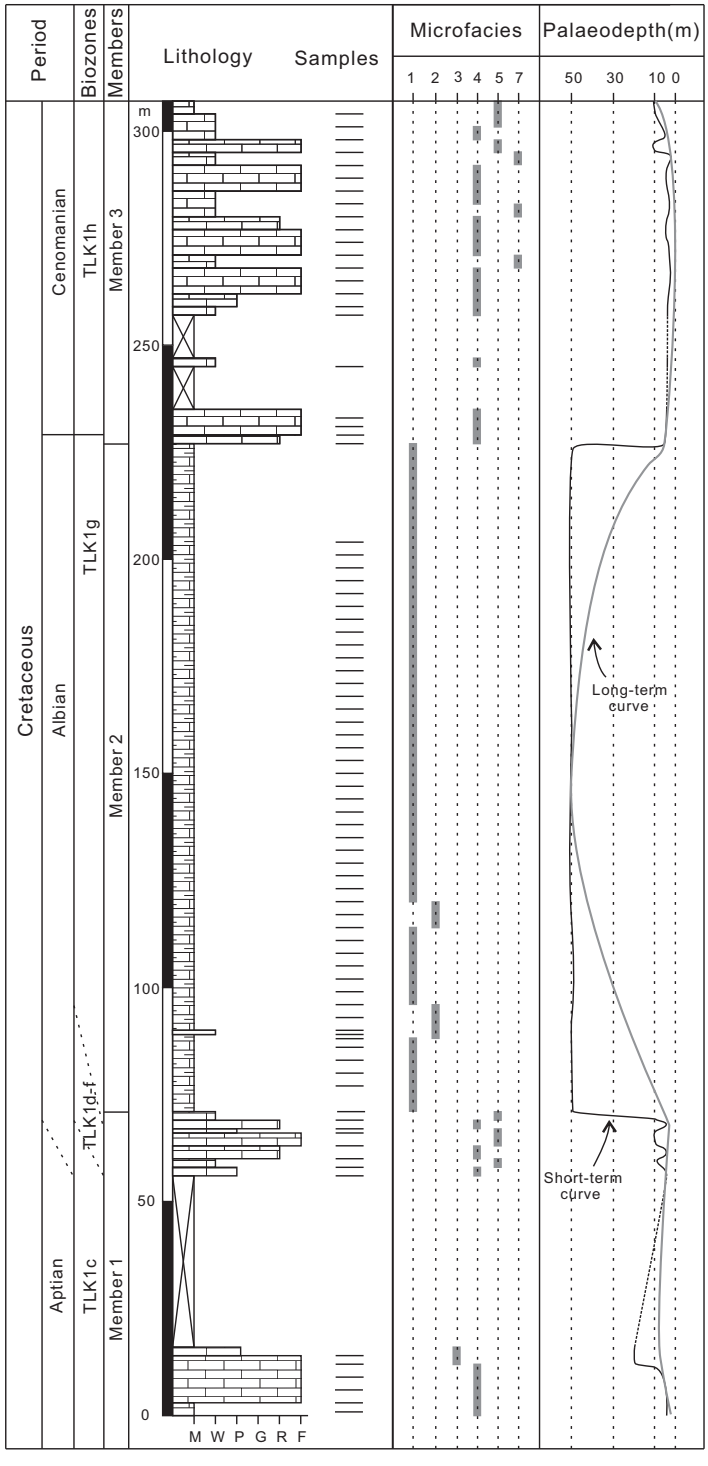

Fig. 7. Stratigraphy and microfacies distribution of the Langshan Formation in the Letie section. In the columns, facies numbered 1–11 refer to the different microfacies. See the text for the descriptions and palaeodepth of microfacies 1–11. The legends are shown in Figure 6.

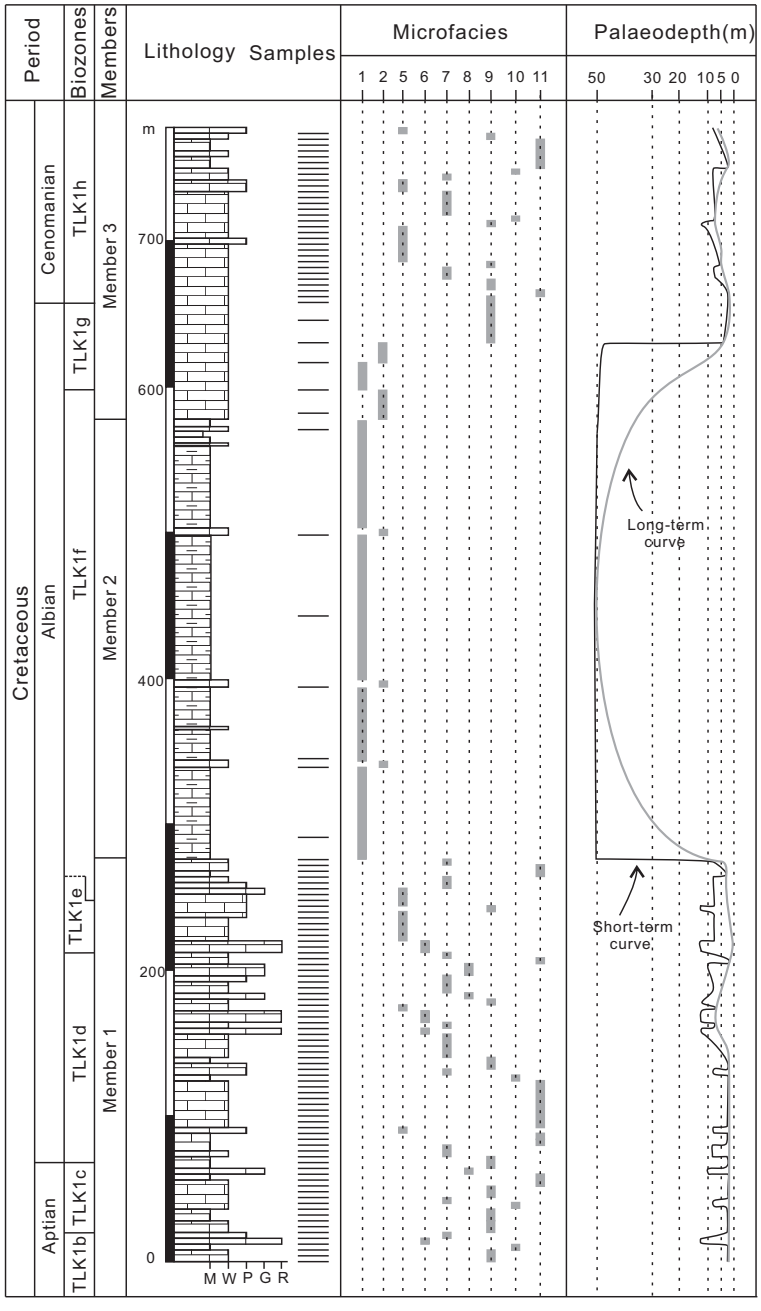

Fig. 8. Stratigraphy and microfacies distribution of the Langshan Formation in the Azhang section. In the columns, facies numbered 1–11 refer to the different microfacies. See the text for the descriptions and palaeodepth of microfacies 1–11. The legends are shown in Figure 6.

foraminifera–rudist wackestone (MF5) in the lower part of the Zulong section, which indicates a rudist bank or back bank environment, and orbitolinids floatstone–rudstone (MF6) in the upper part of the Zulong section, which indicates a deep lagoon with water depths of 10–50 m (Fig. 6).

Member 2 comprises calcispheres wackestone and planktonic foraminiferal wackestone (MF1 and

MF2) in three studied sections, which indicate an open marine environment with water depths of *c.* 50–100 m. However, there was a shallowing event in the middle part of the Zulong section represented by the deposition of green algae packstone (MF7), bioclastic grainstone (MF8) and small benthic foraminifera wackestone–mudstone (MF11) of a shallow lagoon environment (Fig. 6).

The depositional environment of the lowest part of Member 3 in the Azhang section is the same as Member 2 from an open marine environment (Fig. 8). The upper part of Member 3 in the Azhang section is similar to Member 3 in the Letie section, both being dominated by benthic foraminifera–rudist wackestone (MF5), green algae packstone (MF7) and orbitolinids wackestone with small benthic foraminifera (MF9) that formed in a back bank to shallow lagoon environment (Fig. 7). In the Zulong section, Member 3 is dominated by coral rudstone (MF3) and rudist rudstone (MF4) that formed in a forebank patchy reef to rudist bank environment (Fig. 6).

A carbonate platform may have four basic different geometries that may be suitable for the depositional environment of the Langshan Formation: (1) carbonate ramp (gently sloping shelf with water depths steadily increasing basinward); (2) rimmed shelf with a reef or carbonate bank along its outer margin; (3) isolated platform surrounded by deep waters; and (4) epeiric platform with width more than 100 km (Tucker & Wright 1990). Abundant terrigenous detritus within the Langshan Formation has been reported (Sun *et al.* 2017), indicating that the carbonate platform for the Langshan carbonates was not an isolated one. From the Xiagezi section (situated in the southernmost area of the distribution of the Langshan Formation) (Sun *et al.* 2017) to the Letie section (situated in the northernmost area of the distribution of the Langshan Formation) (Fig. 1b), the width of the modern distribution of the Langshan Formation is about 110 km (Fig. 1b). Considering that the Lhasa terrane has experienced north–south shortening of over 55% (Kapp *et al.* 2007), the original width of the distribution of the Langshan Formation was more than 200 km. Therefore, an epeiric platform is most likely suitable for the deposition of the Langshan Formation.

Previously, Sun *et al.* (2017) suggested a ramp model for deposition of the Langshan Formation, considering that the sedimentary environment of the Langshan Formation in the Azhang section was lagoonal throughout the whole section. However, there are several aspects that do not support the ramp model. First, the width of the distribution of the Langshan Formation is larger than ramp models imply, which is normally less than 100 km (Tucker & Wright 1990). Second, in three studied sections of the Langshan Formation, Member 2 was dominated by MF1 and MF2, which indicated an open marine environment with water depth of 50–100 m. The MF2 contains bioclasts sourced from shallow-water facies. However, a normal carbonate ramp exhibits no shallow-water-derived clasts in deeper-water outer ramp deposits (Flügel 2010). Third, in the studied sections, the vertical transition from MF3–4 to MF1–2 clearly shows a drastic water depth change for more than 40 m, which indicates drastic laterally palaeobathymetric changes based on Walther's law (Fig. 9). During the Albian 3–4 (106.7–100.5 Ma), when Member 2 was deposited in the studied sections, the open marine environment (MF 1 and MF2) is restricted to the Azhang–Letie–Zulong areas (Fig. 1), while the Langshan Formation in both the Guolong and the Xiagezi sections (BouDagher-Fadel *et al.* 2017; Sun *et al.* 2017) south of the Azhang–Letie sections and the Xiongmei–Baigoin areas east of the Azhang section (our own unpublished data) (Fig. 1) were deposited in shallow-water lagoon environments. This palaeogeographic distribution also indicates a morphology of flat-topped platforms with drastic water depth changes at its margin rather than a gently sloping ramp topography. Therefore, the carbonate ramp model is not suitable for explaining the deposition of Member 2 of the Langshan Formation.

The major Late Albian transgressive event and comparison with other marine successions

The evolution of carbonate microfacies documents one common deepening event in the Langshan Formation, roughly corresponding to the Member 1/Member 2 boundary in the Azhang and Letie sections, and the middle part/upper part of Member 2 in the Zulong section (Fig. 10). Detailed microfacies analysis clearly shows that, during this deepening event, the water depth changed by more than 40 m, and the biostratigraphy analysis demonstrates this deepening event at the Azhang section to have begun within the benthic foraminiferal biozone TLK1f (*c.* 107 Ma) and continued to TLK1g. In the Letie section, there is a deepening event reconstructed which also continued to TLK1g. The onset of this deepening event is loosely defined to the biozones of TLK1d–TLK1f owing to the lack of planktonic foraminifera within the lower part of Member 2. Considering the same tectonic setting of the Azhang and Letie sections, and that the distance between the two sections is *c.* 50 km, the deepening event found in the Letie section is probably the same deepening event within the TLK1f in the Azhang section. In the Zulong section, there are two deepening events. The first began within TLK1d, while the second occurred during the transition from the middle part to the upper part of Member 2, which can be constrained to benthic foraminiferal biozones TLK1e–f. Comparing these

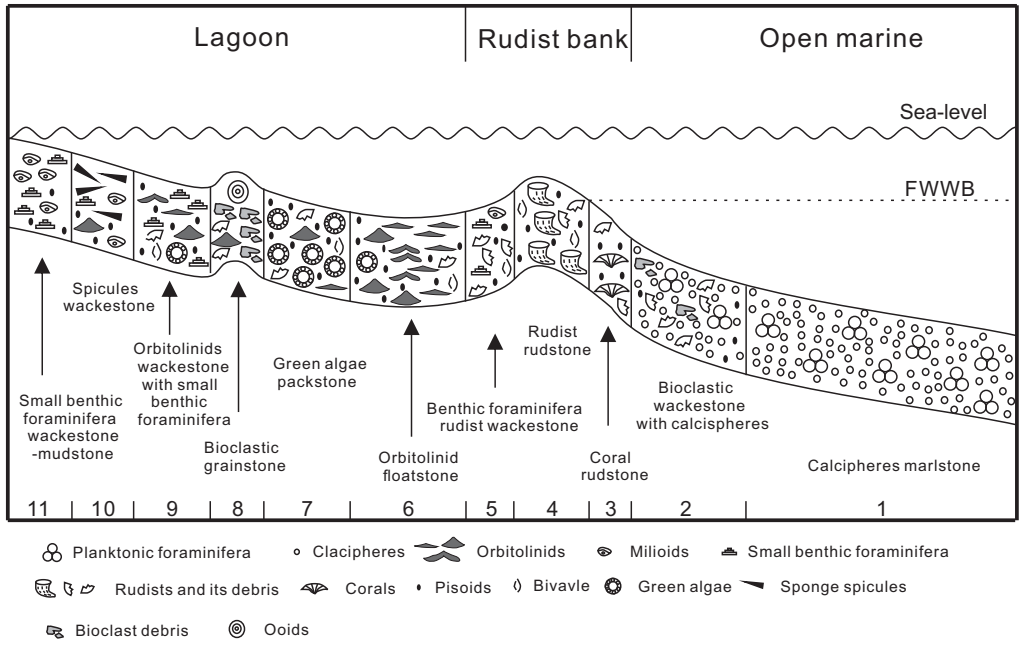

Fig. 9. Depositional model for Member 2 of the Langshan Formation. The numbers in the lower part are codes of microfacies. Abbreviation: FWWB, Fair-weather wave base.

events in the three studied sections, the regional deepening event most likely began within the TLK1f biozone.

The late Albian transgressive event of the Langshan Formation is not limited to central Tibet, but can be traced from the Tethyan Himalaya to the Israel range of the western Tethys, the Russian platform, the Arabian platform and the Western European basins. The Tethyan Himalaya was located on the northern Indian passive continental margin at a palaeolatitude of 40° S during the mid-Cretaceous (Ma *et al.* 2016). The late Albian transgressive event occurred within the planktonic foraminiferal zone of *Rotalipora subticinensis* and was documented by the transition volcaniclastic sandstones in a storm-affected shelf environment to mudstone in pelagic environment (Premoli Silva *et al.* 1992; Garzanti 1993; Hu *et al.* 2010). In the western Tethys, the Israel range was situated at a low palaeolatitude of 10° N during the Cretaceous (Segev *et al.* 2002). The late Albian transgressive event occurred within the planktonic foraminiferal zones *T. breggiensis* to *R. ticinensis* and is evidenced by the transition from shallow-water limestone to shale deposition in a basin environment, with a change in the species diversity of ostracods and a change in the shape of foraminifera from non-keeled to keeled (Flexer *et al.* 1986). The late Albian transgressive event on the Russian platform, which had a palaeo-latitude of 50–70° N, occurred within the ammonite zone *Mortoniceras pricei*, and is evidenced by an exposed unconformity surface overlying shale deposits rich in radiolarian and planktonic foraminifera (Sahagian *et al.* 1996). The relative sea-level changes from the Arabian platform reconstructed by Haq & Al-Qahtani (2005) showed a transgressive event starting at *c.* 107 Ma. A major maximum flooding surface named K100 has been discovered and dated to *c.* 106 Ma. The depositional sequences in the Western European basins showed a transgressive event between the AL8 and AL9 sequence boundary, which occurs within the ammonite zone of *M. pricei* (Hardenbol *et al.* 1998). A sequence stratigraphy correlation by Haq (2014) also showed a transgressive event between the KAl4 and KAl5 sequence boundaries which correlates with the ammonite zone of *M. pricei*.

Based on the Cretaceous biostratigraphy and chronostratigraphy (Ogg & Hinnov 2012), the ammonite zone *M. pricei* can be correlated with the planktonic foraminiferal zone *R. subticinensis* (= *Pseudothalmanninella subticinensis*). The *R. subticinensis* zone, including the *T. breggiensis–R. ticinensis* zone, can be correlated with the Tethyan benthic foraminiferal zone of TLK1f (BouDagher-Fadel 2018*a*) (Fig. 10). Although the duration of these three biozones is shorter than that of TLK1f, the lower boundaries of these four biozones are

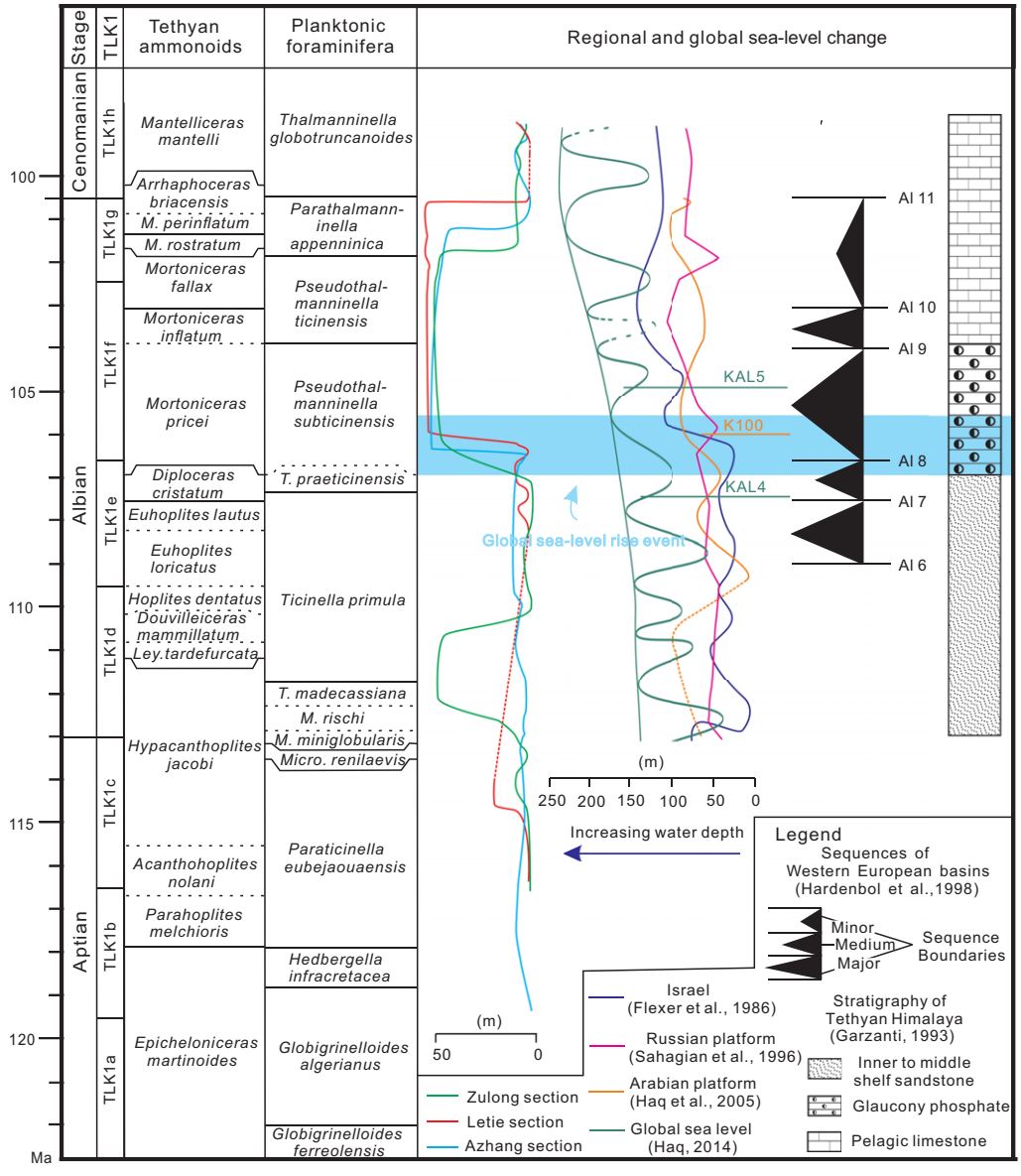

Fig. 10. Comparison of relative sea-level or palaeodepth curves for the mid-Cretaceous. The relative sea-level change of Israel is taken from Flexer *et al.* (1986), that on the Russian platform is from Sahagian *et al.* (1996), that on the Arabian platform is from Haq & Al-Qahtani (2005), the global sea-level change is from Haq (2014) and the sequences of Western European basins are from Hardenbol *et al.* (1998). The change of lithology in Tethyan Himalaya is based on Garzanti (1993). The Tethyan ammonite zone and planktonic foraminiferal zone are adapted from Ogg & Hinnov (2012).

almost synchronous. The observed transgressive events occurred only within the base of this time interval, and we can infer that the deepening event recorded in the Langshan Formation was most likely a global transgressive event at *c.* 107 Ma according to the age correlations of Ogg & Hinnov (2012).

Controlling factors of the Late Albian transgressive event

Global sea-level oscillations on a several-million-year scale are mainly controlled by oceanic spreading and crustal production rates, large igneous

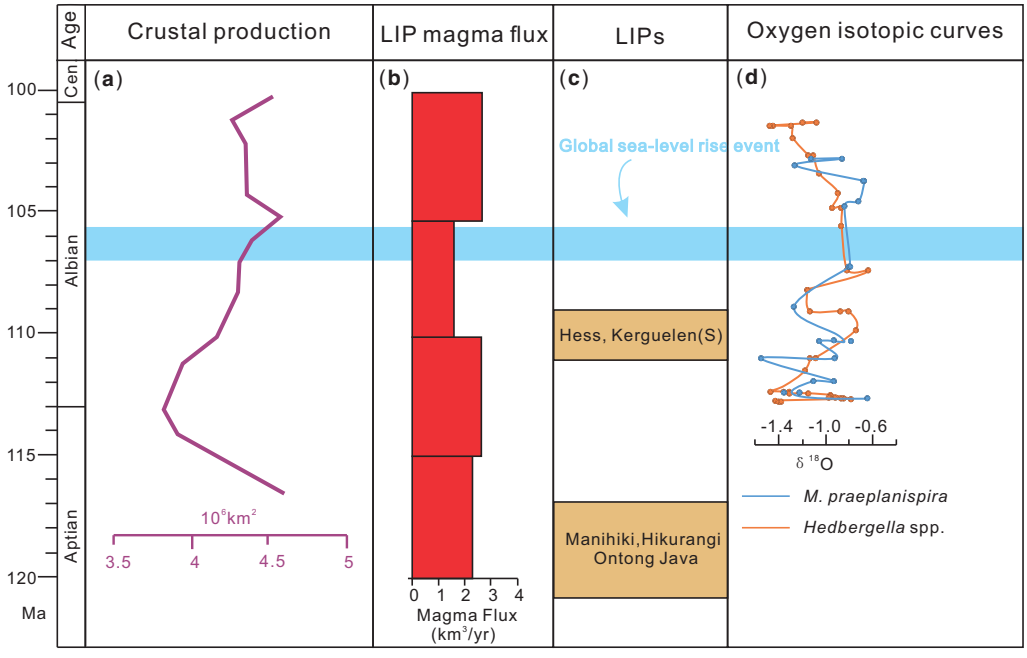

Fig. 11. (**a**) Oceanic crustal production in the mid-Cretaceous (modified after Müller *et al.* 2008). (**b**) Large igneous province magma production during the mid-Cretaceous (modified after Coffin *et al.* 2006); (**c**) Major large igneous provinces of the mid-Cretaceous (modified after Müller *et al.* 2008); (**d**) The mid-Cretaceous oxygen isotope data from different planktonic foraminifera species (the data for *Hedbergella* spp. are from Fassell & Bralower 1999, and the data for *M. praeplanispira* are from Huber *et al.* 2018).

provinces (LIP) eruption and changes in ocean water volume (Miller *et al.* 2011; Conrad 2013; Sames *et al.* 2016). However, oceanic spreading and crustal production rates and LIP eruptions are ruled out because there were no drastic changes in ocean crust production rate and LIP magma flux in the late Albian (Coffin *et al.* 2006; Müller *et al.* 2008) (Fig. 11); therefore, the late Albian transgressive event was most likely controlled by the change in seawater volume, which is mainly controlled by the exchange of water between the oceans and the continents.

Two mechanisms have been proposed to interpret the changes in oceanic water volume in the mid-Cretaceous. The first mechanism is based on the existence of a transient ice sheet in the interior of the Antarctic continent (Miller *et al.* 2003; Haq 2014; Haq & Huber 2017). The growth and decay of the ice sheet could have cause high-frequency and low-amplitude sea-level changes and negative shifts in seawater oxygen isotopic composition. However, during the mid-Cretaceous, the polar temperature was much higher than it is now; thus, the existence of ice sheets is highly improbable (MacLeod *et al.* 2013; O'Brien *et al.* 2017; Huber *et al.* 2018) and there is a lack of direct evidence of an ice sheet during the late Albian (e.g. Alley *et al.* 2019).

The second proposed mechanism for continental water storage is based on the hypothesis that the accelerated hydrological cycle has changed the volume of continental aquifers (lake and underground water), which could account for the third-order sea-level changes (Hay & Leslie 1990; Sames *et al.* 2016; Wendler & Wendler 2016; Hay 2017). Based on the model proposed by Wendler & Wendler (2016), the release of groundwater to the oceans will cause a positive shift of the oxygen isotopic composition of seawater. A previous correlation of Turonian lake-level change to global sea-level change shows an interesting result (Wagreich *et al.* 2014). The high lake level corresponds to the lowest global sea-level, which may indicate that changes in continental aquifers control the eustatic changes during hothouse times. The lack of accurate data on changes in continental aquifers during the Albian period hampers us recognizing the influence of continental aquifers. However, the oxygen isotope of seawater shows that there was little shift from 107 to 105 Ma (Fassell & Bralower 1999; Huber *et al.* 2018) (Fig. 11), which may have been caused by the interaction between the decay of ice sheets and

the release of water from continental aquifers. Therefore, we cannot confirm whether the late Albian transgressive event was controlled by a possible minor polar ice sheet or the change of continental aquifer related to accelerated hydrological processes.

Conclusion

A detailed biostratigraphic and sedimentological study of over 640 thin sections from the Langshan limestone in central Tibet reveals 11 distinct microfacies corresponding three distinct depositional settings. Members 1 and 3 of the Langshan Formation were deposited in a rudist bank to lagoon environment whereas Member 2 was deposited within an open marine environment.

The reconstructed palaeodepth curves define a sudden deepening event from a shallow bank to an open marine setting with an amplitude of *c.* 40 m at *c.* 107 Ma, broadly concurrent with similar events identified in the Tethyan Himalaya, Israel, Russian platform, Arabian platform and Western European basins. This deepening event was a widespread, roughly synchronous feature across the globe, and was controlled by a global sea-level change that may have been related to the decay of an unknown polar ice sheet or release of water from continental aquifer.

Acknowledgments We thank Jiapeng Ye for his assistantance in the field and Zhicheng Huang, Xianghui Li and Zhong Han for their help in the laboratory. This study was financially supported by the National Natural Science Funds for Distinguished Young Scholar (no. 41525007) and the National Natural Science Foundation of China Project (nos 41472081, 91755209). We are grateful for helpful advice and constructive suggestions from anonymous reviewers and to the guest editor Michael Wagreich for the careful handling of our manuscript. This paper is a contribution to UNESCO-IUGS IGCP project 609 "Climate-environmental deteriorations during greenhouse phases: Causes and consequences of short-term Cretaceous sea-level changes".

Funding Award group ID: ID0ESRBG1082, Funding Source: National Natural Science Funds for Distinguished Young Scholar, Funder ID: http://dx.doi.org/10.13039/501100005153, Award ID: 41525007, Principal-award-recipient: Xiumian Hu; Award group ID: ID0EMVBG1083, Funding Source: National Natural Science Foundation of China, Funder ID: http://dx.doi.org/10.13039/501100001809, Award ID: 41472081, Principal-award-recipient: Xiumian Hu; Award group ID: ID0EGZBG1084, Funding Source: National Natural Science Foundation of China, Funder ID: http://dx.doi.org/10.13039/501100001809, Award ID: 91755209, Principal-award-recipient: Xiumian Hu.

Author contributions YX: Writing – Original Draft (Lead); XH: Writing – Original Draft (Supporting), Writing – Review & Editing (Lead); MB-F: Methodology (Supporting), Writing – Review & Editing (Supporting); GS: Investigation (Supporting), Methodology (Supporting); WL: Investigation (Supporting), Methodology (Supporting); JL: Writing – Original Draft (Supporting), Writing – Review & Editing (Equal); SZ: Writing – Review & Editing (Supporting).

References

Alley, N.F., Hore, S.B. & Frakes, L.A. 2019. Glaciations at high-latitude Southern Australia during the Early Cretaceous. *Australian Journal of Earth Sciences*, 1–51, https://doi.org/10.1080/08120099.2019.1590457

Alsharhan, A.S. 1995. Facies variation, diagenesis, and exploration potential of the Cretaceous rudist-bearing carbonates of the Arabian Gulf. *AAPG Bulletin*, **79**, 531–550.

Banner, F.T. & Simmons, M.D. 1994. Calcareous algae and foraminifera as water-depth indicators: an example from the Early Cretaceous carbonates of northeast Arabia. *In*: Simmons, M.D. (ed.) *Micropalaeontology and Hydrocarbon Exploration in the Middle East*. Chapman and Hall, London, 243–252.

BouDagher-Fadel, M.K. 2015. *Biostratigraphic and Geological Significance of Planktonic Foraminifera* (updated 2nd edition). UCL Press, London.

BouDagher-Fadel, M.K. 2018*a*. *Evolution and Geological Significance of Larger Benthic Foraminifera*. UCL Press, London, UK.

BouDagher-Fadel, M.K. 2018*b*. Revised diagnostic first and last occurrences of Mesozoic and Cenozoic planktonic foraminifera. *UCL Office of the Vice-Provost Research, Professional Papers Series*, **2**, 1–5.

BouDagher-Fadel, M.K., Hu, X.M., Price, G.D., Sun, G.Y., Wang, J.G. & An, W. 2017. Foraminiferal biostratigraphy and palaeoenvironmental analysis of the mid-Cretaceous limestones in the southern Tibetan plateau. *Journal of Foraminiferal Research*, **47**, 188–207, https://doi.org/10.2113/gsjfr.47.2.188

Burg, J.P., Proust, F., Tapponnier, P. & Chen, G.M. 1983. Deformation phases and tectonic evolution of the Lhasa block (southern Tibet, China). *Eclogae Geologicae Helvetiae*, **76**, 643–665.

Chen, W., Yang, T. *et al.* 2012. Paleomagnetic results from the Early Cretaceous Zenong Group volcanic rocks, Cuoqin, Tibet, and their paleogeographic implications. *Gondwana Research*, **22**, 461–469, https://doi.org/10.1016/j.gr.2011.07.019

Cisne, J.L. & Gildner, R.F. 1988. Measurement of sea-level change in epeiric seas: the Middle Ordovician transgression in the North American midcontinent. *In*: *Sea-Level Changes – An Integrated Approach*. SEPM, Tulsa, Special Publications, **42**, 217–226.

Cisne, J.L., Gildner, R.F. & Rabe, B.D. 1984. Epeiric sedimentation and sea-level: synthetic ecostratigraphy. *Lethaia*, **17**, 267–288, https://doi.org/10.1111/j.1502-3931.1984.tb00673.x

Coffin, M.F., Duncan, R.O. *et al.* 2006. Large igneous provinces and scientific ocean drilling: status quo and

a look ahead. *Oceanography*, **19**, 150–160, https://doi.org/10.5670/oceanog.2006.13

Cohen, K.M., Finney, S.C., Gibbard, P.L. & Fan, J.-X. 2013. The ICS International Chronostratigraphic Chart. *Episode*, **36**, 199–204, http://www.stratigraphy.org/index.php/icschart-timescale

Conrad, C.P. 2013. The solid Earth's influence on sea-level. *Geological Society of America Bulletin*, **125**, 1027–1052, https://doi.org/10.1130/B30764.1

Davies, R.B., Casey, D.M., Horbury, A.D., Sharland, P.M. & Simmons, M.D. 2002. Early to Mid-Cretaceous mixed carbonate–clastic shelfal systems: examples, issues and models from the Arabian Plate. *GeoArabia*, **7**, 541–598.

DeCelles, P.G. & Kapp, P. 2007. Late Cretaceous to Mid-Tertiary basin evolution in the Central Tibetan Plateau: changing environments in response to tectonic partitioning, aridification, and regional elevation gain. *Geological Society of America Bulletin*, **119**, 654–680, https://doi.org/10.1130/B26074.1

Dunham, R.J. 1962. Classification of carbonate rocks according to depositional texture. *AAPG Memoirs*, **1**, 108–121.

Embry, A.F. & Klovan, J.E. 1971. A late Devonian reef tract on northeastern Banks Island, NWT. *Bulletin of Canadian Petroleum Geology*, **19**, 730–781.

England, P. & Searle, M. 1986. The Cretaceous–Tertiary deformation of the Lhasa block and its implications for crustal thickening in Tibet. *Tectonics*, **5**, 1–14, https://doi.org/10.1029/TC005i001p00001

Fassell, M.L. & Bralower, T.J. 1999. Warm, equable mid-Cretaceous: stable isotope evidence. *Geological Society of America Special Papers*, **332**, 121–142.

Fernández-Mendiola, P.A., Mendicoa, J., Hernandez, S., Owen, H.G. & García-Mondéjar, J. 2013. A facies model for an Early Aptian carbonate platform (Zamaia, Spain). *Facies*, **59**, 529–558, https://doi.org/10.1007/s10347-012-0315-3

Flexer, A., Rosenfeld, A., Lipson-Benitah, S. & Honigstein, A. 1986. Relative sea-level changes during the Cretaceous in Israel. *AAPG Bulletin*, **70**, 1685–1699.

Flügel, E. 2010. *Microfacies of Carbonate Rocks: Analysis, Interpretation and Application*. 2nd edn. Springer, New York.

Garzanti, E. 1993. Sedimentary evolution and drowning of a passive margin shelf (Giumal Group; Zanskar Tethys Himalaya, India): palaeoenvironmental changes during final break-up of Gondwanaland. *In*: Treloar, P.J. & Searle, M.P. (eds) *Himalayan Tectonics*. Geological Society, London, Special Publications, **74**, 277–298, https://doi.org/10.1144/GSL.SP.1993.074.01.20

Ghabeishavi, A., Vaziri-Moghaddam, H., Taheri, A. & Taati, F. 2010. Microfacies and depositional environment of the Cenomanian of the Bangestan anticline, SW Iran. *Journal of Asian Earth Sciences*, **37**, 275–285, https://doi.org/10.1016/j.jseaes.2009.08.014

Gili, E., Masse, J. & Skelton, P.W. 1995. Rudists as gregarious sediment-dwellers, not reef-builders, on Cretaceous carbonate platforms. *Palaeogeography, Palaeoclimatology, Palaeoecology*, **118**, 245–267, https://doi.org/10.1016/0031-0182(95)00006-X

Gold, D.P., White, L.T., Gunawan, I. & BouDagher-Fadel, M.K. 2017. Relative sea-level change in western New Guinea recorded by regional biostratigraphic data. *Marine and Petroleum Geology*, **86**, 1133–1158, https://doi.org/10.1016/j.marpetgeo.2017.07.016

Gradstein, F.M., Ogg, J.G., Schmitz, M.D. & Ogg, G.M. (eds) 2012. *The Geological Time Scale 2012*. Elsevier, Amsterdam, **2**.

Haq, B.U. 2014. Cretaceous Eustasy revisited. *Global and Planetary Change*, **113**, 44–58, https://doi.org/10.1016/j.gloplacha.2013.12.007

Haq, B.U. & Al-Qahtani, A.M. 2005. Phanerozoic cycles of sea-level change on the Arabian Platform. *GeoArabia*, **10**, 127–160.

Haq, B.U. & Huber, B.T. 2017. Anatomy of a eustatic event during the Turonian (Late Cretaceous) hot greenhouse climate. *Science China Earth Sciences*, **60**, 20–29, https://doi.org/10.1007/s11430-016-0166-y

Hardenbol, J., Thierry, J., Farley, M.B., Jacquin, T., Graciansky, P.-C. & Vail, P.R. 1998. Mesozoic and Cenozoic sequence chronostratigraphic framework of European basins. *In*: Graciansky, C.-P., Hardenbol, J., Jacquin, T. & Vail, P.R. (eds) *Mesozoic and Cenozoic Sequence Stratigraphy of European Basins*. SEPM, Tulsa, Special Publications, **60**, 3–13.

Hay, W.W. 2017. Toward understanding Cretaceous climate – an updated review. *Science China Earth Sciences*, **60**, 5–19, https://doi.org/10.1007/s11430-016-0095-9

Hay, W.W. & Leslie, M.A. 1990. Could possible changes in global groundwater reservoir cause eustatic sea-level fluctuations? *In*: Revelle, R. (ed.) *Sea-Level Change*. National Academy Press, Washington, DC, 161–170.

Heckel, P.H. 1972. Recognition of ancient shallow marine environments. *In*: Rigby, J.K. & Hamblin, W.K. (eds) *Recognition of Ancient Sedimentary Environments*, SEPM, Tulsa, Special Publications, **16**, 226–286.

Holland, S.M. 2012. Sea-level change and the area of shallow-marine habitat: implications for marine biodiversity. *Paleobiology*, **38**, 205–217, https://doi.org/10.1666/11030.1

Hu, X.M., Jansa, L., Chen, L., Griffin, W.L., O'Reilly, S.Y. & Wang, J.G. 2010. Provenance of lower Cretaceous Wölong volcaniclastics in the Tibetan Tethyan Himalaya: implications for the final breakup of eastern Gondwana. *Sedimentary Geology*, **223**, 193–205, https://doi.org/10.1016/j.sedgeo.2009.11.008

Huber, B.T., MacLeod, K.G., Watkins, D.K. & Coffin, M.F. 2018. The rise and fall of the Cretaceous Hot Greenhouse climate. *Global and Planetary Change*, **167**, 1–23, https://doi.org/10.1016/j.gloplacha.2018.04.004

Husinec, A. & Jelaska, V. 2006. Relative sea-level changes recorded on an isolated carbonate platform: Tithonian to Cenomanian succession, southern Croatia. *Journal of Sedimentary Research*, **76**, 1120–1136, https://doi.org/10.2110/jsr.2006.099

Immenhauser, A., Schlager, W. *et al.* 1999. Late Aptian to late Albian sea-level fluctuations constrained by geochemical and biological evidence (Nahr Umr Formation, Oman). *Journal of Sedimentary Research*, **69**, 434–446, https://doi.org/10.2110/jsr.69.434

Kapp, P., DeCelles, P.G., Leier, A.L., Fabijanic, J.M., He, S., Pullen, A. & Gehrels, G.E. 2007. The Gangdese retroarc thrust belt revealed. *GSA Today*, **17**, 4–9, https://doi.org/10.1130/GSAT01707A.1

KAYA, M.Y. & ALTINER, D. 2015. Microencrusters from the Upper Jurassic–Lower Cretaceous İnaltı Formation (Central Pontides, Turkey): remarks on the development of reefal/peri-reefal facies. *Facies*, **61**, 18, https://doi.org/10.1007/s10347-015-0445-5

KOMINZ, M.A., BROWNING, J.V., MILLER, K.G., SUGARMAN, P.J., MIZINTSERVA, S. & SCOTESE, C.R. 2008. Late Cretaceous to Miocene sea-level estimates from the New Jersey and Delaware coastal plain coreholes: an error analysis. *Basin Research*, **20**, 211–226, https://doi.org/10.1111/j.1365-2117.2008.00354.x

LAI, W., HU, X.M., GARZATI, E., SUN, G.Y., GARZIONE, C.N., BOUDAGHER-FADEL, M.K. & MA, A.L. 2019*a*. Initial growth of the Northern Lhasaplano in the early late Cretaceous (92 Ma). *Geological Society of America Bulletin*, **131**, 1823–1836, https://doi.org/10.1130/B35124.1

LAI, W., HU, X.M., GARZANTI, E., XU, Y.W., MA, A.L. & LI, W. 2019*b*. Early Cretaceous sedimentary evolution of the northern Lhasa terrane and the timing of initial Lhasa–Qiangtang collision. *Gondwana Research*, **73**, 136–152, https://doi.org/10.1016/j.gr.2019.03.016

LEIER, A.L., DECELLES, P.G., KAPP, P. & GEHRELS, G.E. 2007*a*. Lower Cretaceous Strata in the Lhasa Terrane, Tibet, with Implications for Understanding the Early Tectonic History of the Tibetan Plateau. *Journal of Sedimentary Research*, **77**, 809–825, https://doi.org/10.2110/jsr.2007.078

LEIER, A.L., DECELLES, P.G., KAPP, P. & DING, L. 2007*b*. The Takena Formation of the Lhasa terrane, southern Tibet: the record of a Late Cretaceous retroarc foreland basin. *Geological Society of America Bulletin*, **119**, 31–48, https://doi.org/10.1130/B25974.1

LEIER, A.L., KAPP, P., GEHRELS, G.E. & DECELLES, P.G. 2007*c*. Detrital zircon geochronology of Carboniferous–Cretaceous strata in the Lhasa Terrane, Southern Tibet. *Basin Research*, **19**, 361–378, https://doi.org/10.1111/j.1365-2117.2007.00330.x

MA, Y., YANG, T., BIAN, W., JIN, J., ZHANG, S., WU, H. & LI, H. 2016. Early Cretaceous paleomagnetic and geochronologic results from the Tethyan Himalaya: insights into the Neotethyan paleogeography and the India–Asia collision. *Scientific Reports*, **6**, 21605, https://doi.org/10.1038/srep21605

MA, Y., YANG, T., BIAN, W., JIN, J., WANG, Q., ZHANG, S. & WU, H. 2018. A stable Southern Margin of Asia during the Cretaceous: paleomagnetic constraints on the Lhasa–Qiangtang collision and the maximum width of the Neo-Tethys. *Tectonics*, **37**, 3853–3876, https://doi.org/10.1029/2018TC005143

MACLEOD, K.G., HUBER, B.T., BERROCOSO, Á.J. & WENDLER, I. 2013. A stable and hot Turonian without glacial $\delta^{18}O$ excursions is indicated by exquisitely preserved Tanzanian foraminifera. *Geology*, **41**, 1083–1086, https://doi.org/10.1130/G34510.1

MASSE, J.P. 1992. The Lower Cretaceous Mesogean benthic ecosystems: palaeoecologic aspects and palaeobiogeographic implications. *Palaeogeography, Palaeoclimatology, Palaeoecology*, **91**, 331–345, https://doi.org/10.1016/0031-0182(92)90075-G

MILLER, K.G., SUGARMAN, P.J. *ET AL.* 2003. Late Cretaceous chronology of large, rapid sea-level changes: glacioeustasy during the greenhouse world. *Geology*, **31**, 585–588, https://doi.org/10.1130/0091-7613(2003)031<0585:LCCOLR>2.0.CO;2

MILLER, K.G., KOMINZ, M.A. *ET AL.* 2005. The Phanerozoic record of global sea-level change. *Science*, **310**, 1293–1298, https://doi.org/10.1126/science.1116 412

MILLER, K.G., MOUNTAIN, G.S., WRIGHT, J.D. & BROWNING, J.V. 2011. A 180-million-year record of sea-level and ice volume variations from continental margin and deep-sea isotopic records. *Oceanography*, **24**, 40–53, https://doi.org/10.5670/oceanog.2011.26

MÜLLER, R.D., SDROLIAS, M., GAINA, C., STEINBERGER, B. & HEINE, C. 2008. Long-term sea-level fluctuations driven by ocean basin dynamics. *Science*, **319**, 1357–1362, https://doi.org/10.1126/science.1151540

O'BRIEN, C.L., ROBINSON, S.A. *ET AL.* 2017. Cretaceous sea-surface temperature evolution: constraints from TEX86 and planktonic foraminiferal oxygen isotopes. *Earth-Science Reviews*, **172**, 224–247, https://doi.org/10.1016/j.earscirev.2017.07.012

OGG, J.G. & HINNOV, L.A. 2012. Cretaceous. *In*: GRADSTEIN, F.M., OGG, J.G., SCHMITZ, M.D. & OGG, G.M. (eds) *The Geologic Time Scale*. Elsevier, Oxford, 793–853.

PAN, G.T., DING, J., YAO, D.S. & WANG, L.Q. 2004. *Guide Book of 1:1,500,000 Geologic Map of the Qinghai-Xizang (Tibet) Plateau and Adjacent Areas*. Chengdu Cartographic Publishing House, Chengdu, China.

PREMOLI SILVA, I., GARZANTI, E. & GAETANI, M. 1992. Stratigraphy of the Chikkim and Fatu La Formations in the Zangla and Zumlung Units (Zanskar Range, India) with comparisons to the Thakkhola region (central Nepal): Mid-Cretaceous evolution of the Indian passive margin. *Rivista Italiana di Paleontologia e Stratigrafia. Rivista Italiana di Paleontogia e Stratigrafia*, **97**, 511–564, https://doi.org/10.13130/2039-4942/8961

RAMKUMAR, M. 2015. *Cretaceous Sea-level Rise: Down Memory Lane and the Road Ahead*. Elsevier.

RAO, X., SKELTON, P.W., SHA, J., CAI, H. & IBA, Y. 2015. Mid-Cretaceous rudists (Bivalvia: Hippuritida) from the Langshan Formation, Lhasa block, Tibet. *Papers in Palaeontology*, **1**, 401–424, https://doi.org/10.1002/spp2.1019

SAHAGIAN, D., PINOUS, O., OLFERIEV, A. & ZAKHAROV, V. 1996. Eustatic curve for the Middle Jurassic–Cretaceous based on Russian platform and Siberian stratigraphy: zonal resolution. *AAPG Bulletin*, **80**, 1433–1458.

SAMES, B., WAGREICH, M. *ET AL.* 2016. Short-term sea-level changes in a greenhouse world – a view from the Cretaceous. *Palaeogeography, Palaeoclimatology, Palaeoecology*, **441**, 393–411, https://doi.org/10.1016/j.palaeo.2015.10.045

SEGEV, A., SASS, E., RON, H., LANG, B., KOLODNY, Y. & MCWILLIAMS, M. 2002. Stratigraphic, geochronologic, and paleomagnetic constraints on Late Cretaceous volcanism in northern Israel. *Israel Journal of Earth Sciences*, **51**, 297–309, https://doi.org/10.1560/VUTP-RNR5-UU08-Y7WT

STEIN, M., ARNAUD-VANNEAU, A. *ET AL.* 2012. Palaeoenvironmental and palaeoecological change on the northern Tethyan carbonate platform during the Late Barremian to earliest Aptian. *Sedimentology*, **59**,

939–963, https://doi.org/10.1111/j.1365-3091.2011.01286.x

Sun, G.Y., Hu, X.M., Sinclair, H.D., BouDagher-Fadel, M.K. & Wang, J.G. 2015. Late Cretaceous evolution of the Coqen Basin (Lhasa terrane) and implications for early topographic growth on the Tibetan Plateau. *Geological Society of America Bulletin*, **127**, 1001–1020, https://doi.org/10.1111/j.1365-3091.2011.01286.x

Sun, G.Y., Hu, X.M. & Sinclair, H.D. 2017. Early Cretaceous palaeogeographic evolution of the Coqen Basin in the Lhasa Terrane, southern Tibetan Plateau. *Palaeogeography Palaeoclimatology Palaeoecology*, **485**, 101–118, https://doi.org/10.1130/B31137.1

Tucker, M.E. & Wright, V.P. 1990. *Carbonate Sedimentology*. Blackwell Science, Oxford.

Wagreich, M., Lein, R. & Sames, B. 2014. Eustasy, its controlling factors, and the limno-eustatic hypothesis – concepts inspired by Eduard Suess. *Austrian Journal of Earth Science*, **107**, 115–131.

Wang, J.G., Hu, X.M., Garzanti, E., An, W. & Liu, X.C. 2017*a*. The birth of the Xigaze forearc basin in southern Tibet. *Earth and Planetary Science Letters*, **465**, 38–47, https://doi.org/10.1016/j.epsl.2017.02.036

Wang, J.G., Hu, X., Garzanti, E., Ji, W.Q., Liu, Z.C., Liu, X.C. & Wu, F.Y. 2017*b*. Early cretaceous topographic growth of the Lhasaplano, Tibetan plateau: constraints from the Damxung conglomerate. *Journal of Geophysical Research: Solid Earth*, **122**, 5748–5765, https://doi.org/10.1002/2017JB014278

Wendler, J.E. & Wendler, I. 2016. What drove sea-level fluctuations during the mid-Cretaceous greenhouse climate? *Palaeogeography, Palaeoclimatology, Palaeoecology*, **441**, 412–419, https://doi.org/10.1016/j.palaeo.2015.08.029

Wilson, J.L. 1975. *Carbonate Facies in Geologic History*. Springer, New York.

Yin, A. & Harrison, T.M. 2000. Geologic Evolution of the Himalayan–Tibetan Orogen. *Annual Review of Earth and Planetary Sciences*, **28**, 211–280, https://doi.org/10.1146/annurev.earth.28.1.211

Zaghbib-Turki, D. 2003. Cretaceous coral–rudist formations in Tunisia. *In*: Gili, E. *et al.* (eds) *Paleogeography and Paleoecology*. North African Cretaceous Carbonate Platform Systems, 83–110.

Zhang, K.J. 2000. Cretaceous paleogeography of Tibet and adjacent areas (China): tectonic implications. *Cretaceous Research*, **21**, 23–33, https://doi.org/10.1006/cres.2000.0199

Zhang, K.J., Xia, B.D., Wang, G.M., Li, Y.T. & Ye, H.F. 2004. Early Cretaceous stratigraphy, depositional environments, sandstone provenance, and tectonic setting of central Tibet, western China. *Geological Society of America Bulletin*, **116**, 1202–1222, https://doi.org/10.1130/B25388.1

Zhang, K.J., Zhang, Y., Tang, X. & Xia, B. 2012. Late Mesozoic tectonic evolution and growth of the Tibetan plateau prior to the Indo-Asian collision. *Earth-Science Reviews*, **114**, 236–249, https://doi.org/10.1016/j.earscirev.2012.06.001

Zhang, Q.H., Ding, L., Cai, F., Xu, X., Zhang, L., Xu, Q. & Willems, H. 2011. Early Cretaceous Gangdese retroarc foreland basin evolution in the Selin Co basin, central Tibet: evidence from sedimentology and detrital zircon geochronology. *In*: Gloaguen, R. & Ratschbacher, L. (eds) *Growth and Collapse of the Tibetan Plateau*. Geological Society, London, Special Publications, **353**, 27–44, https://doi.org/10.1144/SP353.3